NUMERICAL ANALYSIS OF THE INFLUENCE OF AN AUXILIARY OSCILLATING MAGNETIC FIELD ON SUPPRESSING THE POROSITY FORMATION IN DEEP PENETRATION LASER BEAM WELDING OF ALUMINUM ALLOYS

F. YANG*, X. MENG*, M. BACHMANN*, A. ARTINOV*,
S. N. PUTRA*, M. RETHMEIER**, *, ***

**Bundesanstalt für Materialforschung und prüfung (BAM), Unter den Eichen 87, 12205 Berlin, Germany*
***Institute of Machine Tools and Factory Management, Technische Universität Berlin, Pascalstraße 8-9, 10587 Berlin, Germany ***Fraunhofer Institute for Production Systems and Design Technology, Pascalstraße 8-9, 10587 Berlin, Germany*

DOI 10.3217/978-3-85125-968-1-13

ABSTRACT

The contactless magnetohydrodynamic technology has been considered as a potential and promising method to improve the weld qualities of deep penetration laser beam welding. In this paper, numerical investigations are conducted to study the influence of the auxiliary oscillating magnetic field on the porosity suppression in laser beam welding of 5754 aluminum alloy. To obtain a deeper insight into the suppression mechanism, a three-dimensional transient multi-physical model is developed to calculate the heat transfer, fluid flow, keyhole dynamic, and magnetohydrodynamics. A ray tracing algorithm is employed to calculate the laser energy distribution on the keyhole wall. A time-averaged downward Lorentz force is produced by an oscillating magnetic field. This force acts in the molten pool, leading to a dominant downward flow motion in the longitudinal section, which blocks the bubble migration from the keyhole tip to the rear part of the molten pool. Therefore, the possibility for the bubbles to be captured by the solidification front is reduced. The electromagnetic expulsive force provides an additional upward escaping speed for the bubbles of 1 m/s ~ 5 m/s in the lower and middle region of the molten pool. The simulation results are in a good agreement with experimental measurements. Based on the results obtained in this study, a better understanding of the underlying physics in laser beam welding enhanced by an auxiliary oscillating magnetic field can be provided and thus the welding process can be further optimized reducing the porosity formation.

Keywords: Deep penetration laser beam welding; Oscillating magnetic field; Numerical simulation; Porosity; Molten pool behaviour.

INTRODUCTION

Deep penetration laser beam welding (LBW) has been developed as a promising technology with numerous applications in joining thick plates above 5 mm [1]. Compared

to traditional arc welding, deep penetration LBW shows more advantages including large aspect ratio, high welding speed, narrow heat affected zone, and low weld distortion [2]. Based on the above-mentioned advantages, wide applications of this technology have been achieved in joining thick plates of aluminum alloy.

However, porosities are commonly observed in the LBWed joints of aluminum alloys, which result in deterioration of the welded joints' quality and reliability [3,4]. The porosities in LBWed joints can be classified as the so-called metallurgical and process porosity [5]. The metallurgical porosity is not the main emphasis of this study which is caused by the elements with low boiling-point from base metal and moisture in the atmosphere or shielding gas. Process porosity induced by keyhole instability with a size larger than 100 μm has been drawing more and more attention. The formation of the process porosity can be mainly ascribed to the keyhole collapse, dynamic melt flow behind the keyhole, and high solidification rate [6-9]. Furthermore, researchers have investigated many suppression methods of process porosity during deep penetration LBW. For example, the methods of using different shielding gases [9], changing the angle of incident laser beam [10], conducting welding under vacuum [11], applying hybrid welding [12], and performing welding coupled with oscillating laser beam [13] have been investigated in detail.

Recently, contactless magnetohydrodynamic (MHD) technology has been recognized as a potential way to improve the deep penetration LBW, which can control the flow pattern of melting liquid by the induced Lorentz force from external magnetic fields. The welding quality can be improved based on multiple effects of braking, supporting, and stirring achieved by different Lorentz force application methods performed with multiple types of magnetic fields (steady magnetic field or oscillating magnetic field) and magnetic field directions [14-16]. Moreover, researchers found that external magnetic fields can suppress process porosity significantly. Huang et al. [17] reported that the porosity defect is eliminated obviously by using an auxiliary steady magnetic field during laser beam welding of steel. The reasons limiting porosity formation by the steady magnetic field are mainly related to the increased stability of the keyhole, the larger bubble escape speed, and the lower solidification rate of the weld pool. Fritzsche et al. [18] applied a transverse oscillating magnetic field in a partial penetration LBW of aluminum. Significant porosity suppression of more than 70% and better surface stabilization were achieved.

Although the effect of the external magnetic fields on the porosity suppression have been verified by experiments, a deeper insight into the relationships between magnetic fields, keyhole dynamics, and process porosity is harder to obtain because of the non-transparent molten metal and the small diameter of the keyhole. Moreover, the fluid flow behaviour in the molten pool is highly nonlinear, which makes the quantitative experimental analysis difficult. Therefore, multi-physical modeling is a powerful tool to investigate the physical interaction mechanisms between keyhole dynamics, process porosity, and MHD behaviour. Recently, a few researchers have developed three dimensional multi-physical models to investigate the formation of porosity, in which the Volume of Fluid method (VOF) was applied to capture the free surface of the keyhole [6, 8]. Furthermore, some numerical models were established with consideration of external magnetic field. Zhang et al. [19] built a three-dimensional transient numerical model to investigate the influence mechanism of an alternating magnetic field on the weld root hump suppression in full penetration laser welding of aluminum. Meng et al. [20]

investigated the highly transient keyhole dynamics under a magnetic field by using multi-physical modeling. The correlation between the porosity mitigation and molten pool dynamics effected by magnetic field was elucidated in detail. Liu et al. [21] studied the influence of the magnetic field orientation on suppressing porosity by establishing a numerical model coupled with MHD. They found the keyhole stability was well improved when the magnetic fields were horizontally parallel and perpendicular to the welding direction.

However, further quantitative analysis of the interaction mechanisms between keyhole dynamics, process porosity, and MHD behaviour during deep penetration LBW is still lacking. In the present study, a 3D transient multi-physical numerical model, coupled with the VOF algorithm and a MHD model, has been developed to investigate this interaction mechanism. The weld pool behaviour is analysed under the influence of the Lorentz force and the corresponding suppression mechanism of the magnetic field on process porosity during deep penetration LBW is discussed.

EXPERIMENTAL PROCEDURE

The experiments of butt welding were conducted by an IPG YLR 20000 laser welding system. The welding parameters used in the experiments are listed in Table 1. The 5754 aluminum alloy was used as base metal with dimensions of 200 mm × 50 mm × 10 mm. The laser beam was inclined in a forward direction with an angle of 10°. Pure Ar was used as shielding gas with a flow rate of 20 l/min, which was placed in the backward direction with an angle of 15°. A high-speed camera was used to capture the temporal evolution of the molten pool from a side view with a frequency of 1000 frames/s. The molten pool depth, width, and length extracted from the experimental results are used for the verification of the numerically obtained results. The experimental platform is shown in Fig. 1 (a).

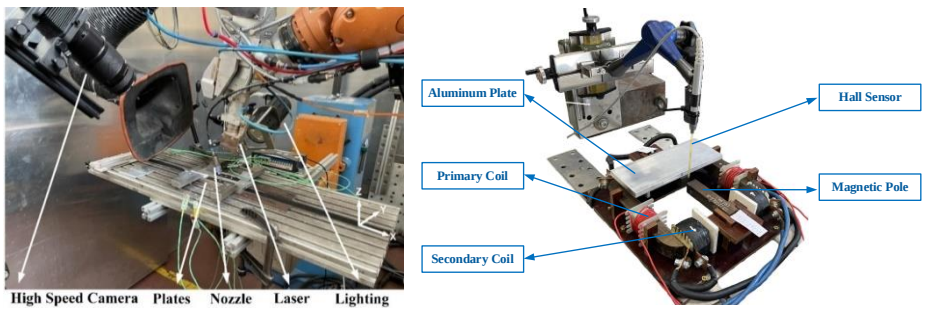

Fig. 1 Experimental setup: (a) laser beam welding platform; (b) Measurement platform of magnetic fields distribution in the cold material

The oscillating magnetic field are produced by an in-house developed alternating current (AC) electromagnet. The dimension of the cross-section of the magnetic pole is 20 mm × 20 mm and the distance between the two magnetic poles is 15 mm. In order to simplify the model, the generation of the external magnetic field is not considered in this model. Therefore, the magnetic field was measured by a Hall sensor in a cold condition

before the laser was turned on and it was applied directly in this model, the measurement platform is shown in Fig.1 (b). The peak magnetic flux density produced by this oscillating magnetic system is 220 mT and the frequency is 1830 Hz, which is used in this numerical model. Fig. 2 shows the spatial distribution of magnetic flux density.

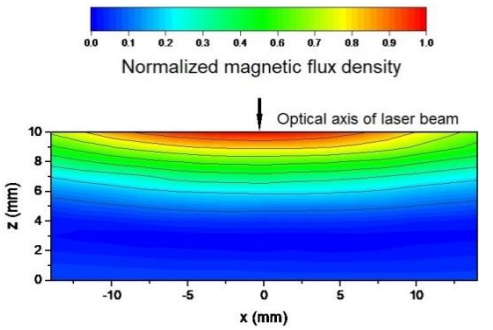

Fig. 2 Normalized magnetic flux density (Frequency: 1830 Hz, Peak magnetic flux density: 220 mT)

The joints were cut perpendicular to the weld seam by mechanical cutting and subsequently the cross-section of samples was polished and etched by 2.5 ml HNO3 + 1.5 ml HCl + 1 ml HF + 95 ml H_2O. The fusion line shape in the cross-section was observed by an optical microscope.

Table 1 Welding parameters in experiments and simulation

Parameters	Value
Laser power	5 kW
Laser spot diameter at focal plane	520 μm
Wavelength	1070 nm
Focal length	350 mm
Focal position	0 mm
Welding speed	2 m/min

MATHEMATICAL MODELING

A three-dimensional transient multi-physical model accounting for the VOF method and MHD has been developed to calculate the heat transfer, fluid flow, and the keyhole dynamics. Some simplifications are applied to reduce the computing costs because of the highly complex and multi-physical coupled fluid flow behavior in the molten pool. The assumptions are as follows:

- The flow regime of the liquid metal flow is laminar. The liquid metal is considered as Newtonian and incompressible. The buoyance term follows the Boussinesq approximation.

- The metal vapor in the keyhole is weakly ionized, thereby the gaseous phase in the model is considered electrically non-conductive.
- The effect of shielding gas is neglected in the simulation.
- The thermoelectric effect and the Joule heating are not taken into consideration.

GOVERNING EQUATIONS

Based on the assumptions, the governing equation in a fixed Cartesian coordinates system can be mathematically described as following:

- VOF equation

$$\frac{\partial \phi}{\partial t} + \nabla \cdot (\vec{v}\phi) = 0, \tag{1}$$

where ϕ is the volume fraction of aluminum, t is the time and $\vec{v} = (v_x,\ v_y,\ v_z)$ is the fluid velocity vector.

- Mass conservation

$$\nabla \cdot \vec{v} = 0. \tag{2}$$

- Energy conservation

$$\rho\left[\frac{\partial h}{\partial t} + (\vec{v} \cdot \nabla)h\right] = \nabla \cdot (k\nabla T) + S_q, \tag{3}$$

where h is the enthalpy, k is the thermal conductivity, and S_q is the energy source term. All surface energies are converted to volumetric energies by the continuum surface force method because of the application of the VOF method [22]. This additional source terms consider the laser heat flux density, the convective and radiative heat transfer, the evaporation loss, and the recondensation.

- Navier-stokes equation

$$\rho\left(\frac{\partial \vec{v}}{\partial t} + (\vec{v} \cdot \nabla)\vec{v}\right) = -\nabla p + \mu\nabla^2\vec{v} + \rho\vec{g} - \beta\rho(T - T_L)\vec{g} - \mu K\vec{v} + \overrightarrow{S_m}, \tag{4}$$

where ρ is the density, p is the hydrodynamic pressure, μ is the viscosity, $\vec{g}$ is the gravitational acceleration vector, T is the temperature, T_L is the liquidus temperature, K is the Carman-Kozeny equation [23]. The effects of surface tension along the aluminum-air interface, the recoil pressure induced by evaporation, the stagnation pressure and shear stress on the keyhole surface are as well converted into volumetric forces and implemented into the additional momentum source $\overrightarrow{S_m}$.

- Magnetic induction equation

The magnetic induction equation can be written as following according to Ohm's law and Maxwell's equation:

$$\frac{\partial \vec{b}}{\partial t} + (\vec{v} \cdot \nabla)\vec{b} = \frac{1}{\mu_m \sigma_e}\nabla^2\vec{b} + \left(\left(\overrightarrow{B_0} + \vec{b}\right) \cdot \nabla\right)\vec{v} - (\vec{v} \cdot \nabla) \cdot \overrightarrow{B_0}, \tag{5}$$

where $\vec{b}$ is the magnetic field induced by the liquid flow, $\overrightarrow{B_0}$ is an external magnetic field measured by a Hall sensor, μ_m is the magnetic permeability, and σ_e is the electrical conductivity. The induced current density $\vec{j}$ and Lorentz force $\overrightarrow{F_L}$ are written as the following:

$$\vec{j} = \frac{1}{\mu_m} \nabla \times (\overrightarrow{B_0} + \vec{b}), \tag{6}$$

$$\overrightarrow{F_L} = \vec{j} \times (\overrightarrow{B_0} + \vec{b}), \tag{7}$$

The Lorentz force is then introduced as part of the momentum source term.

PHYSICAL MODELS

The laser beam profile is assumed to have a Gaussian-like axisymmetric distribution, which can be expressed as follows:

$$q_L = \frac{2P_L}{\pi r_z^2} \cdot \exp(-2\frac{x^2+y^2}{r_z^2}), \tag{8}$$

$$r_z = r_f \left[1 + \left(\frac{z-z_f}{z_r}\right)^2\right]^{\frac{1}{2}}, \tag{9}$$

where q_L denotes the heat density function, P_L is the laser power, r_z is the radius of the laser beam at z distance away from the focal plane, x and y are the coordinates, z_f is the position of the focal plane, r_f is the laser beam radius at the focal plane.

In this model, a ray tracing algorithm developed by Cho et al. is applied to calculate the ray reflections [24]. For this purpose, the laser beam energy is discretized into several energy bundles. Meanwhile, finer secondary virtual cells on the keyhole wall are used to improve the accuracy of the ray tracing algorithm. Note that this virtual approach comes without significant increase of the calculating time [20, 25, 26]. The Fresnel absorption happened during every reflection can be calculated by the following equation:

$$\alpha = 1 - \frac{1}{2}\left(\frac{1+(1-\varepsilon cos\varphi)^2}{1+(1+\varepsilon cos\varphi)^2} + \frac{\varepsilon^2 - 2\varepsilon cos\varphi + 2cos^2\varphi}{\varepsilon^2 + 2\varepsilon cos\varphi + 2cos^2\varphi}\right), \tag{10}$$

where φ is the angle between the incident ray and the surface normal, ε is a coefficient determined by the laser type and the material properties, which is set as 0.087 in this model [27].

The recoil pressure due to evaporation is described as follows [28]:

$$P_r = 0.54 P_0 \exp(l_v M \frac{T-T_b}{RTT_b}), \tag{11}$$

where P_r is the recoil pressure, P_0 is the atmospheric pressure, l_v is the latent heat of vaporization, M is the atomic mass, T_b is the boiling temperature, and R is the universal gas constant.

The normal capillary pressure P_{ca} and the tangential Marangoni stress τ_{ma} can be written as:

$$P_{ca} = \gamma\kappa, \tag{12}$$

$$\tau_{ma} = \frac{\partial\gamma}{\partial T}\frac{\partial T}{\partial \vec{s}}, \tag{13}$$

where γ is the surface tension of aluminum [8], κ and $\vec{s}$ are the curvature and the tangential vector of keyhole surface, respectively.

In addition, the influence of thermal (secondary heating q_{plume} and recondensation q_{recond}) and momentum from high-speed metal vapor (stagnation pressure P_{sta} and shear stress τ_{vap}) on the keyhole are also considered in this model [24,29].

BOUNDARY CONDITION

The energy balance on the keyhole wall can be described as:

$$-k\frac{\partial T}{\partial \vec{n}} = q_L - h_c(T - T_0) - \sigma\varepsilon_r(T^4 - T_0^4) - \rho v_{evp}\Delta L_v + q_{plume} + q_{recond}, \tag{14}$$

where $\vec{n}$ is the normal vector of the free surface, h_c is the coefficient of the convective heat transfer, T_0 is the ambient temperature, σ is the Stefan-Boltzmann constant, v_{evp} is the recession speed of the free surface.

The force balance on the keyhole wall can be written as:

$$-p + 2\mu\frac{\partial v_n}{\partial \vec{n}} = p_r + p_{sta} + p_{ca} \tag{15}$$

$$-\mu\frac{\partial v_t}{\partial \vec{n}} = \tau_{ma} + \tau_{vap} \tag{16}$$

where v_n is the normal velocity and v_t is the tangential velocity. Eq. (15) describes the force balance in normal direction and the force balance in tangential direction can be expressed by Eq. (16).

Another energy and electromagnetic boundary conditions are shown in Table 2. The continuum boundary condition is applied on the side face of the geometry model to allow for realistic and accurate description of the thermal and electromagnetic conduction in a semi-infinite domain.

Table 2 Energy and electromagnetic boundary conditions

	Energy	**Electromagnetic**
Top	$\partial T/\partial \vec{n}$=0	$\vec{j}$=0
Side aluminum surface	Continuum boundary [30]	Continuum boundary [30]
Side gas surface	$\partial T/\partial \vec{n}$=0	$\vec{j}$=0
Bottom	$-k\,\partial T/\partial \vec{n} = -h_c(T - T_0)$ $-\sigma\varepsilon_r(T^4 - T_0^4)$	$\vec{j}$=0

The initial conditions are:

$$T|_{t=0} = 300\ K, \vec{v}|_{t=0} = 0, \vec{b}\big|_{t=0} = 0 \tag{17}$$

NUMERICAL SETUP

Fig. 3 shows the schematic of the computational domain. The dimensions of the geometric model are 20 mm × 8 mm × 12 mm, the gas phase layer with 2 mm thickness is built above the workpiece. A uniform hexahedral cell size of 0.2 mm was used to discretize the computational domain.

All transport equations are solved with the commercial software ANSYS FLUENT. The discretization of the momentum and energy conservation equations was done by a second order upwind algorithm. The velocity-pressure coupling is achieved by the Pressure Implicit with Splitting of Operators (PISO) method. The aluminum-air interface is reconstructed by the Geo-Reconstruct method. The simulation was calculated by a high-performance computing cluster in the Bundesanstalt für Materialforschung und prüfung (BAM) with 80 CPU cores and 768 GB RAM. About 96 h computational time were consumed to simulate 0.45 s physical welding time.

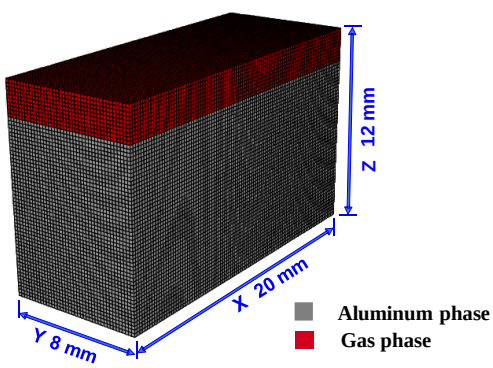

Fig. 3 Schematic of computational domain

RESULTS AND DISCUSSION

EXPERIMENT RESULTS AND VALIDATION

Severe porosity defects can be identified from the longitudinal section of the LBWed joints of 5754 aluminum alloy, see Fig.4. The porosity shown in the dashed rectangle (I, II) is typical keyhole-induced process pores, whose shape can be either spherical or irregular and the size of these porosities are usually larger than that of metallurgical porosity. According to the research of Fritzsche et al. [18] and Bachmann et al. [31], a

significant reduction of porosity can be achieved by the application of magnetic fields. Therefore, the objectives of the present study focus on the analysis of the suppression mechanism of magnetic fields on keyhole induced process porosity by using the numerical results.

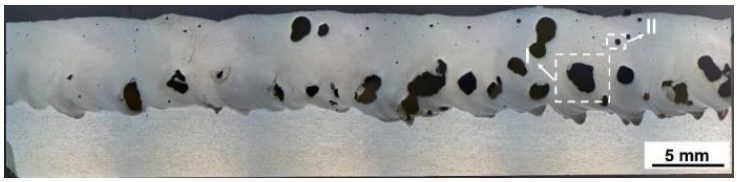

Fig. 4 Longitudinal section of LBWed joints of 5754 aluminum alloy

A series comparison between the experimental and calculated results were conducted. The molten pool on the top surface is typical teardrop shape, which is similar as the numerical result, see Fig. 5. In Fig.6, the dashed line is the profile of the final weld. Table 3 lists the errors between the experimental and the simulated results. From Fig.5, Fig.6 and Table 3, the profile of the calculated fusion zone shows good agreement with the experimental results. The errors between the experimental results and the calculated results are lower than 10%. The above comparison validates the numerical model which can thus be used in the following analysis.

Fig. 5 Comparison between experimental and calculated molten pool length without magnetic fields: (a) experiment results; (b) calculated results (the red region in the simulation result represents the calculated weld region)

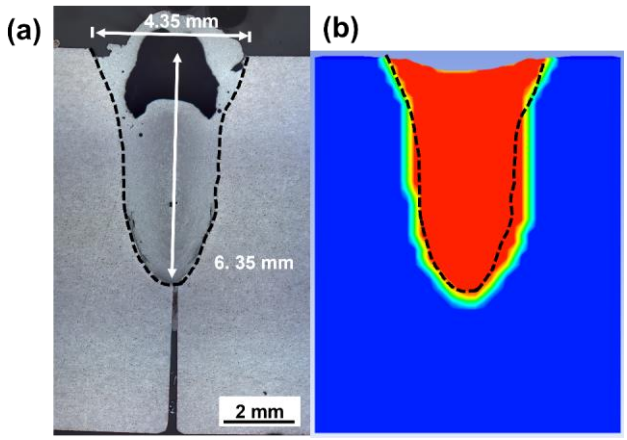

Fig. 6 Comparison between experimental and calculated fusion zones without magnetic fields: (a) experiment results; (b) calculated results (the red region in the simulation result represents the calculated weld region)

Table 3 Deviations between experimental and calculated results without magnetic fields

	Width of molten pool	Length of molten pool	Depth of molten pool
Experiment	4.35 mm	8.52 mm	6.35 mm
Simulation	4.69 mm	7.70 mm	6.75 mm
Errors	8%	10%	6%

ELECTROMAGNETIC BEHAVIOUR

The eddy currents are induced by an oscillating magnetic field in the workpiece, as shown in Fig.7. For a better visualization of the eddy current distribution, the magnitude is normalized by the maximal value. Two predominant circulating currents are found in the longitudinal section. This can be attributed to the fact that the value of the electric conductivity decreases with increasing temperature and the gaseous phase in the keyhole is also assumed as non-conductive. Thus, the keyhole with high temperature and the gaseous phase in the inner keyhole can be regarded as an electric barrier. The eddy current flow can be either clockwise or anti-clockwise, which is determined by the temporal variation of the magnetic flux density. The maximum value of the induced eddy current is 2.5×10^7 A/m^2. This flow pattern of the induced current is similar with the research results of Meng et al. [32]. and Bachmann et al. [33], but the magnitude is much higher due to the high electrical conductivity of aluminum.

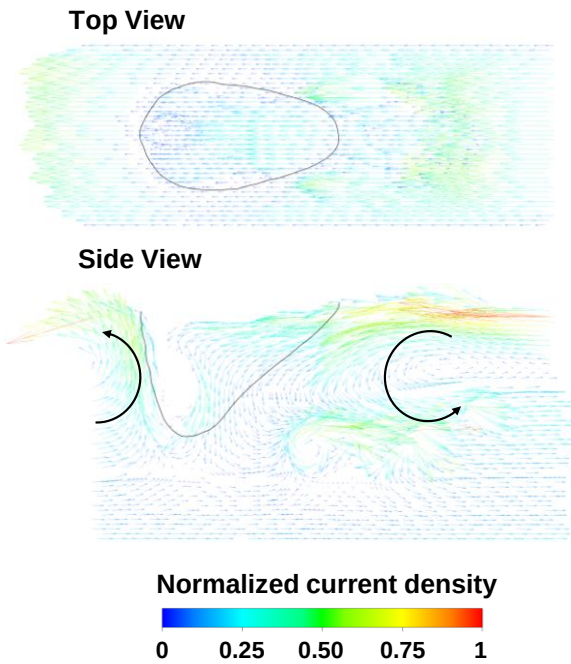

Fig. 7 Vector field of the induced eddy current

The Lorentz force is produced by the oscillating magnetic fields and its self-induced electric current. Intuitively, it shows periodic expansive and compressive effects like the oscillation of the magnetic field. The Lorentz force is the strongest on the top surface of the workpiece due to the maximum magnetic flux density occurred on the top position (see Fig. 2). Because of the skin effect, the induced Lorentz force will reduce sharply along the vertical direction. The Lorentz force in vertical direction at point A is extracted and shown in Fig. 8. The periodical upward and downward Lorentz force oscillates with a frequency of 3660 Hz which is double as high compared to the frequency of the magnetic field. According to Fig. 8, the maximum upward Lorentz force at point A is reached within the range of $1 \sim 3 \times 10^5$ N/m^3.

After ¼ period of the oscillating magnetic field, the maximum downward Lorentz force can be produced with the value of $2.5 \sim 4.5 \times 10^5$ N/m^3. From a time-average viewpoint, the downward Lorentz force can be produced in the molten pool by the oscillating magnetic fields. For the keyhole, the expansive and compressive Lorentz force can as well be produced on the keyhole wall. Meng et al. [20] indicated that the Lorentz force formed on the opening of the keyhole has a significant effect on the laser absorption.

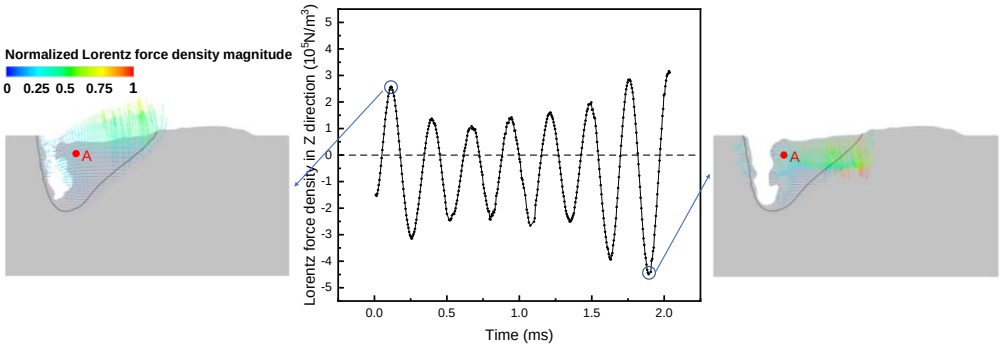

Fig. 8 Distribution of Lorentz force density in molten pool

MOLTEN POOL BEHAVIOUR AND KEYHOLE DYNAMICS

Fig. 9 shows the comparison of the calculated temperature and velocity fields between the LBW and LBW assisted with an external magnetic field after the quasi-steady state is reached. It is considered that the fluid flow pattern in the molten pool has a remarkable effect on the porosity formation. There are two main flow circulations, see Fig. 9, in the well-developed molten pool without a magnetic field. The predominant flow routine of the molten metal in the longitudinal section is marked with white arrows. These two typical flow circulations were as well confirmed by the numerical and experimental research results from Liu et al. [21] and Kawahito et al. [34]. The upper circulation contributes to the formation of the elongated molten pool profile. It should be noted that the thin layer of the liquid metal on the keyhole front wall shows a fast downward flow under the recoil pressure. This downward flow is redirected at the liquid/solid boundary to form the second circulation at the bottom. The existence of the bottom circulation is not stable. It can disappear during the calculation sometimes and be rebuilt by the downward liquid metal from the keyhole wall. It has been found that the bottom circulation plays a crucial role in the formation and migration of the bubbles [6]. The formation of the bubbles can be mainly attributed to the collapse of the keyhole tip. The bottom circulation tends to push the formed bubbles to the solidification front, which increases the possibility of the capture of the bubbles [6,8].

The application of an external magnetic field has a significant impact on the fluid flow pattern in the molten pool. The backward flow at the top region is enhanced by the Lorentz force, and thus both the length and the width of the molten pool is increased. The reason that the keyhole depth decreases after applying the magnetic fields is that the induced Lorentz force changes the energy distribution by affecting the diameter of the keyhole opening and the protrusions' position in keyhole wall [21]. By comparing Fig. 9 (b) and (d), it shows that an apparent downward flow is formed in the longitudinal section due to the time-averaged downward Lorentz force, which brings a suppression on the occurrence of the bottom circulation. This transformation of the flow mode is helpful for suppressing the formation of porosities. The bubble migration routine from the keyhole tip to the rear part of the molten pool is blocked by the enhanced downward fluid flow.

Thus, the possibility of the moving bubble captured by the solidification front can be reduced. The bubble formed in the keyhole tip has more opportunity to re-merge to the keyhole or move upward. Therefore, the process porosity can be suppressed.

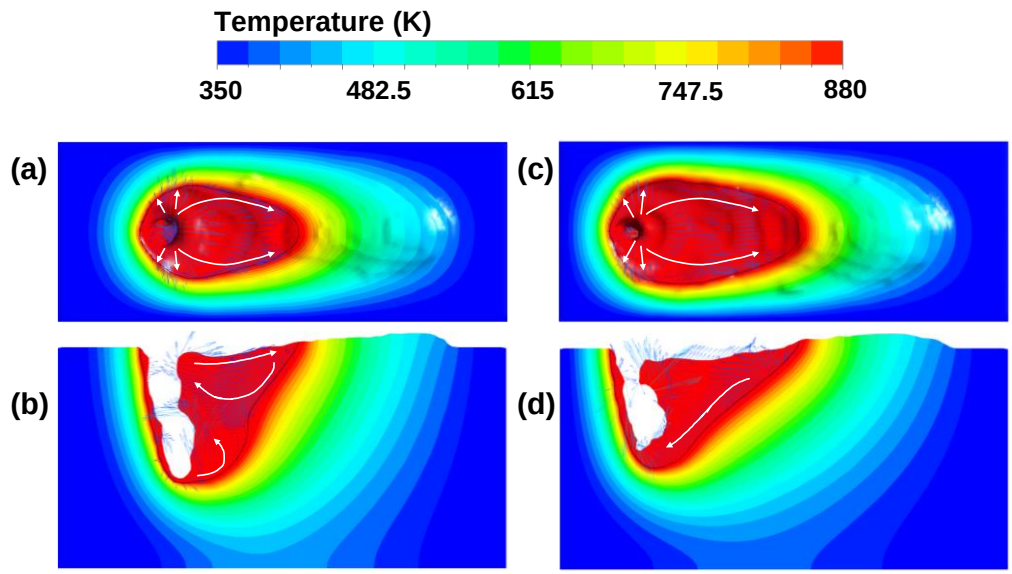

Fig. 9 Calculated temperature and velocity fields ($t = 0.357\ s$): (a) top surface of the molten pool without magnetic field; (b) x-z central surface without magnetic field; (c) top surface of molten pool with magnetic field; (d) x-z central surface with magnetic field

The pressure difference that exists around non-conducting porosities can cause the electromagnetic expulsive forces due to the generation of the Lorentz force. If the liquid metal movement is ignored, the liquid flow will be deemed as Stokes flow. The additional escaping speed provided by the electromagnetic expulsive force can be described as:

$$\frac{3}{4}\frac{\pi d_B^3}{6}F_L = 3\pi\mu d_B v_{esc} \quad [20]$$

The accelerating process of the bubble is ignored, the constant escaping speed contributed by electromagnetic expulsive force can be calculated from this equation when the forces on the bubble are balanced. The term on the left-hand side is the electromagnetic expulsive force proposed by Leenov-Kolin's theory from Takahashi et al. [35]. The term on the right-hand side represents the total drag force on the bubble. Here d_B is the pore diameter (here an average pore diameter of 1.15 mm is chosen according to Fig. 4), F_L is the Lorentz force density, v_{esc} is the upward escaping velocity contributed by the electromagnetic expulsive force. The electromagnetic expulsive force induced by the Lorentz force can provide the bubble an additional escaping velocity in most areas of the molten pool, see Fig. 10. The additional escaping speed is higher on the top region of molten pool because of the maximum Lorentz force there. This larger additional escaping speed in the top region has no higher significance for the bubble escaping. However, the induced electromagnetic expulsive force still provides an additional upward escaping

speed within the range of $1\ \mathrm{m/s} \sim 5\ \mathrm{m/s}$ in the lower and middle part of the molten pool, which is a crucial factor for bubble escaping and suppressing porosity. Thus, the bubbles have more opportunity to escape from the molten pool because of the application of the external oscillating magnetic field. From Fig.4, two typical diameters of pores (Pore I and II) are extracted. Pore I is a single larger pore whose equivalent diameter is 1.92 mm. According to Eq. (20), the larger bubble with diameter of 1.92 mm has an additional upward escaping speed with $3\ \mathrm{m/s} \sim 13\ \mathrm{m/s}$ under the vertical component of Lorentz force of $1.5 \times 10^4\ \mathrm{N/m^3} \sim 6 \times 10^4\ \mathrm{N/m^3}$ in the lower and middle part of the molten pool. However, the smaller bubble (Pore II) with diameter 0.38 mm just be given an additional upward escaping speed within the range of $0.1\ \mathrm{m/s} \sim 0.5\ \mathrm{m/s}$ in the lower and middle region of the molten pool. It means that especially the larger bubbles have more possibilities to escape from molten pool.

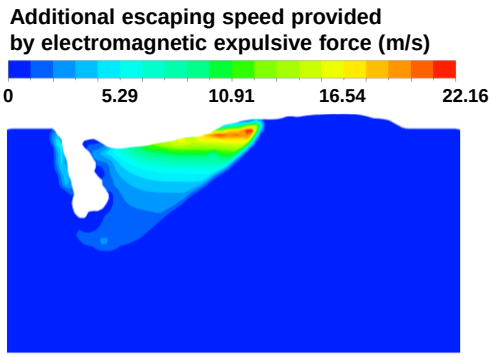

Fig. 10 Additional escaping speed provided by external magnetic expulsive force

A statistical analysis on the keyhole collapse position is conducted, which is given in Fig. 11. 83% of the keyhole collapse happens at the position between $0\ \mathrm{mm} \sim 1\ \mathrm{mm}$ above the keyhole bottom when a magnetic field is applied. The collapse possibility of 78% occurs at the position between $0\ \mathrm{mm} \sim 1\ \mathrm{mm}$ when the LBW conducted without magnetic fields. Moreover, the collapse occurred randomly at the upper and middle part of the keyhole. This distribution result disagrees with the standard normal distribution of keyhole collapse position during the LBW of titanium alloy reported by Pang et al. [36]. It also disobeys log-normal distribution occurred during the LBW process of 304L steel studied by Meng et al. [20]. This phenomenon may be associate to the lower viscosity and surface tension coefficient of molten aluminum alloy compared to steel and titanium alloys. The lower viscosity and surface tension coefficient make the keyhole dynamic behavior changes more significantly and the keyhole collapse occurs more frequently, which may exhibit entirely different dynamic behavior compared to titanium and steel. Therefore, the keyhole dynamic behavior of aluminum alloy LBW with auxiliary magnetic fields requires further investigation.

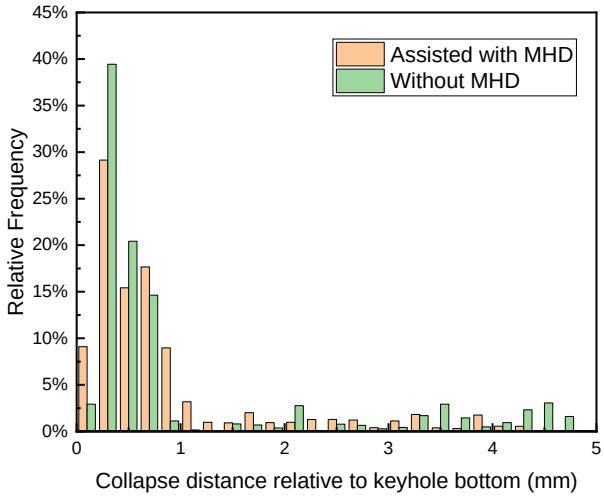

Fig. 11 Probability histogram of the collapse distance relative to keyhole bottom

CONCLUSION

(1) A 3D transient multi-physical LBW model coupled with an external oscillating magnetic field is developed to investigate the relationship between the magnetic fields, keyhole dynamics and process porosity.
(2) The application of external magnetic fields has a strong influence on the molten pool profile and fluid flow pattern. An apparent downward flow is formed in the longitudinal section under the effect of the Lorentz force.
(3) The enhanced downward fluid flow blocks the bubble migration routine from the keyhole tip to the rear part of the molten pool. The possibility of the bubbles captured by the solidification front reduces notably. The electromagnetic expulsive force induced by Lorentz force can provide the bubble with $1\,\mathrm{m/s}$~ $5\,\mathrm{m/s}$ additional upward escaping speed in the lower and middle regions of the molten pool.

ACKNOWLEDGEMENT

This work is funded by China Scholarship Council (Nr. 202008080270) and the Deutsche Forschungsgemeinschaft (DFG, German Research Foundation) project Nr. 411393804 (BA 5555/5-2), Nr. 416014189 (BA 5555/6-1), and Nr. 466939224 (BA 5555/9-1).

References

[1] M. BACHMANN, A. GUMENYUK, M. RETHMEIER: 'Welding with high-power lasers: Trends and developments', *Phys Procedia*, 83, 15-25, 2016.
[2] JF. READY, DF. FARSON, T. FEELEY: *LIA Hand Book of Laser Materials Processing*, 2001.

[3] H. ZHAO, DR. WHITE, T. DEBROY: 'Current issues and problems in laser welding of automotive aluminum alloys', *International Materials Reviews*, 44(6), 238-266, 1999.
[4] S. KATAYAMA, CD. LUNDIN: 'Laser welding of aluminum alloy 5456', *Welding International*, 6(6), 425-435, 1992.
[5] A. MATSUNAWA, JD. KIM, S. KATAYAMA: 'Porosity formation in laser welding-Mechanisms and suppression methods', *International Congress on Applications of Lasers & Electro-Optics*, 1997(1), G73-G82, 1997.
[6] L. HUANG, X. HUA, D. WU, F. LI: 'Numerical study of keyhole instability and porosity formation mechanism in laser welding of aluminum alloy and steel', *Journal of Materials Processing Technology*, 252, 421-431, 2018.
[7] R. ZHANG, X. TANG, L. XU, F. LU, H. CUI: 'Study of molten pool dynamics and porosity formation mechanism in full penetration fiber laser welding of Al-alloy', *International Journal of Heat Mass Transfe*r, 148, 119089, 2020.
[8] R. LIN, H. WANG, F. LU, J. SOLOMON, BE. CARLSON: 'Numerical study of keyhole dynamics and keyhole-induced porosity formation in remote laser welding of Al alloys', *International Journal of Heat and Mass Transfer*, 108, 244-256, 2017.
[9] A. MATSUNAWA, M. MIZUTANI, S. KATAYAMA: 'Porosity formation mechanism and its prevention in laser welding', *Welding International*, 17(6), 431-437, 2003.
[10] N. SETO, S. KATAYAMA, A. MATSUNAWA: 'Porosity formation mechanism and reduction method in CO_2 laser welding of stainless steel', *Welding International*, 16(6), 451-460, 2002.
[11] M. JIANG, X. CHEN, Y. CHEN, W. TAO: 'Increasing keyhole stability of fiber laser welding under reduced ambient pressure', *Journal of Materials Processing Technol*ogy, 268: 213-222, 2019.
[12] M. CHEN, J. XU, L. XIN, Z. ZHAO, F. WU, S. MA, Y. ZHANG: 'Effect of keyhole characteristics on porosity formation during pulsed laser-GTA hybrid welding of AZ31B magnesium alloy', *Optics and Lasers in Engineering*, 93, 139-145, 2017.
[13] W. KE, X. BU, JP. OLIVEIRA, W. XU, Z. WANG, Z. ZENG: 'Modeling and numerical study of keyhole-induced porosity formation in laser beam oscillating welding of 5A06 aluminum alloy', *Optics & Laser Technology*, 133, 106540, 2021.
[14] M. BACHMANN, V. AVILOV, A. GUMENYUK: 'Numerical assessment and experimental verification of the influence of the Hartmann effect in laser beam welding processes by steady magnetic fields', *International Journal of Thermal Sciences*, 101, 24-34, 2016.
[15] VV. AVILOV, A. GUMENYUK, M. LAMMERS, M. RETHMEIER: 'PA position full penetration high power laser beam welding of up to 30 mm thick AlMg3 plates using electromagnetic weld pool support', *Science and Technology of Welding and Joining*, 17(2), 128-133, 2012.
[16] M. GATZEN, Z. TANG, F. VOLLERTSEN, M. MIZUTANI, S. KATAYAMA: 'X-ray investigation of melt flow behavior under magnetic stirring regime in laser beam welding of aluminum', *Journal of Laser Applications*, 23(3), 032002, 2011.
[17] L. HUANG, P. LIU, S. ZHU, X. HUA, S. DONG: 'Experimental research on formation mechanism of porosity in magnetic field assisted laser welding of steel', *Journal of Manufacturing Processes*, 50, 596-602, 2020.
[18] A. FRITZSCHE, K. HILGENBERG, F. TEICHMANN, H. PRIES, K. DILGER, M. RETHMEIER: 'Improved degassing in laser beam welding of aluminum die casting by an electromagnetic field', *Journal of Materials Processing Technology*, 253, 51-56, 2018.
[19] R. ZHANG, X. TANG, L. XU, F. LU, H. CUI: 'Mechanism study of thermal fluid flow and weld root hump suppression in full penetration laser welding of Al alloy with alternating magnetic field support', *International Journal of Heat and Mass Transfer*, 166, 120759, 2021.
[20] X. MENG, M. BACHMANN, A. ARTINOV, M. RETHMEIER: 'A study of the magnetohydrodynamic effect on keyhole dynamics and defect mitigation in laser beam welding', *Journal of Materials Processing Technology*, 307, 117636, 2022.

[21] F. LIU, H. WANG, X. MENG, C. TAN, B. CHEN, X. SONG: 'Effect of magnetic field orientation on suppressing porosity in steady-magnetic-field-assisted aluminum alloy deep-penetration laser welding', *Journal of Materials Processing Technology*, 304, 117569, 2022.
[22] J. BRACKBILL, D. KOTHE, C. ZEMACH: 'A continuum method for modeling surface tension', *Journal of Computational Physics*, 100(2): 335-354, 1992.
[23] V.R. VOLLER, C. PRAKASH: 'A fixed grid numerical modeling methodology for convection-diffusion mushy region phase change problem', *International Journal of Heat and Mass Transfer*, 30, 1709-1719, 1987.
[24] WI. CHO, SJ. NA, C. THOMY, F. VOLLERTSEN: 'Numerical simulation of molten pool dynamics in high power disk laser welding', *Journal of Materials Processing Technology*, 212(1), 262-275, 2012.
[25] SW. HAN, J. AHN, SJ. NA: 'A study on ray tracing method for CFD simulations of laser keyhole welding: progressive search method', *Welding in the World*, 60(2), 247-258, 2016.
[26] X. MENG, A. ARTINOV, M. BACHMANN, Ö. ÜSTÜNDAĞ, A. GUMENYUK, M. RETHMEIER: 'The detrimental molten pool narrowing phenomenon in wire feed laser beam welding and its suppression by magnetohydrodynamic technique', *International Journal of Heat and Mass Transfer*, 193: 122913, 2022.
[27] R. DUCHARME, K. WILLIAMS, P. KAPADIA, J. DOWDEN, B. STEEN, M. GLOWACKI: 'The laser welding of thin metal sheets: an integrated keyhole and weld pool model with supporting experiments', *Journal of Physics D: Applied Physics*, 27(8): 1619, 1994.
[28] M. ALLMEN, A. BLATTER: 'Laser-Beam interactions with materials (second ed.)', *Springer*, New York, 1995.
[29] S. MUHAMMAD, S. HAN, S. NA, A. GUMENYUK, M. RETHMEIER: 'Study on the role of recondensation flux in high power laser welding by computational fluid dynamics simulations', *Journal of Laser Applications*, 30(1), 012013, 2018.
[30] X. MENG, G. QIN, R. ZONG: 'Thermal behavior and fluid flow during humping formation in high-speed full penetration gas tungsten arc welding', *International Journal of Thermal Sciences*, 134, 380-391, 2018.
[31] M. BACHMANN, V. AVILOV, A. GUMENYUK, M. RETHMEIER: 'Experimental and numerical investigation of an electromagnetic weld pool control for laser beam welding', *Physics Procedia*, 56, 515-524, 2014.
[32] X. MENG, M. BACHMANN, A. ARTINOV, M. RETHMEIER: 'The influence of magnetic field orientation on metal mixing in electromagnetic stirring enhanced wire feed laser beam welding', *Journal of Materials Processing Technology*, 294, 117135, 2021.
[33] M. BACHMANN, R. KUNZE, V. AVILOV, M. RETHMEIER: 'Finite element modeling of an alternating current electromagnetic weld pool support in full penetration laser beam welding of thick duplex stainless steel plates', *Journal of Laser Application*, 28(2): 022404, 2016.
[34] Y. KAWAHITO, Y. UEMURA, Y. DOI, M. MIZUTANI, K. NISHIMOTO, H. KAWAKAMI, M. TANAKA, H. FUJI, K. NAKATA, S. KATAYAMA: 'Elucidation of the effect of welding speed on melt flows in high-brightness and high-power laser welding of stainless steel on basis of three dimensional X-ray transmission in situ observation', *Welding International*, 31(3):206-213, 2017.
[35] K. TAKAHASHI, S. TANIGUCHI: 'Electromagnetic separation of nonmetallic inclusion from liquid metal by imposition of high frequency magnetic field', *ISIJ international*, 43(6): 820-827, 2003.
[36] S. PANG, W. CHEN，W. WANG: 'A Quantitative Model of Keyhole Instability Induced Porosity in Laser Welding of Titanium Alloy', *Metallurgical and Materials Transactions A*, 45(6): 2808-2818, 2014.